Supplementary information

Edge-induced Selective Etching of bilayer MoS_2 Kirigami Structure via Space-Confined method

Weijie Ma,[a,b,†] *Qing Zhang,*[a,b,d†] *Jie Zhu,*[a,b] *Yang Guo,*[a,b] *Yajing Sun,*[a,b,f] *Lin Li,*[c,e] *Dechao Geng,*[*,a,b,e,f]

[a.] Key Laboratory of Organic Integrated Circuit, Ministry of Education & Tianjin Key Laboratory of Molecular Optoelectronic Sciences, Department of Chemistry, School of Science, Tianjin 300072, China.

[b.] Collaborative Innovation Center of Chemical Science and Engineering (Tianjin), Tianjin 300072, China.

[c.] College of Chemistry, Tianjin Normal University, Tianjin 300387, China.

[d.] School of Advanced Materials, Peking University Shenzhen Graduate School, Peking University, Shenzhen 518055, China.

[e.]Beijing National Laboratory for Molecular Sciences, Beijing 100190, China.

[f.] Haihe Laboratory of Sustainable Chemical Transformations, Tianjin 300192, China.

† W. Ma and Q. Zhang contributed equally to this work.

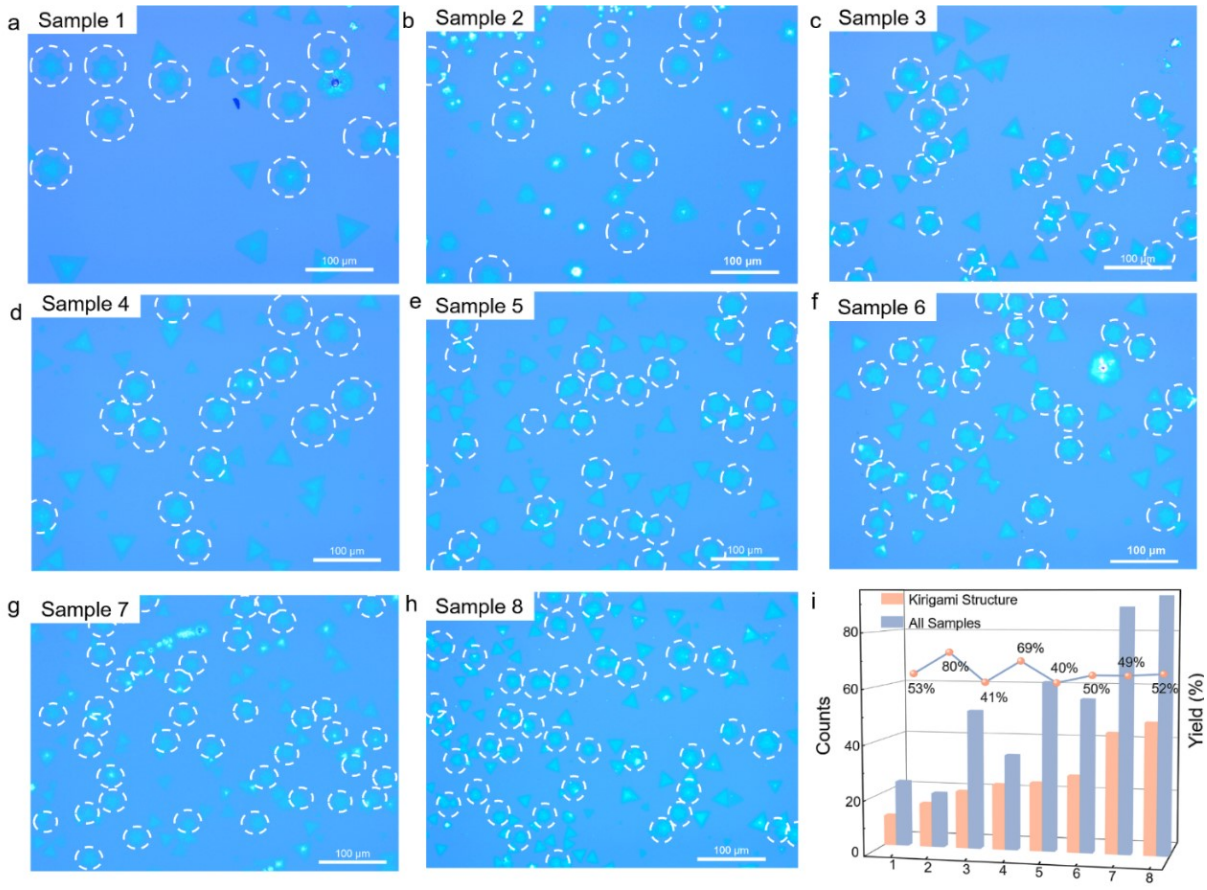

Figure S1. Large-area optical images of MoS_2 kirigami structures obtained from different batches. (a-h) The white dotted circle highlights the kirigami samples. (i) The proportion of the kirigami structure in the visual area. According to statistics, the kirigami structure in different batches of samples reached more than 40%.

We carried out nearly 300 batches under the optimized growth conditions, of which almost 240 batches reproduced the kirigami structure, demonstrating the remarkable repeatability of this space-confined method. Another 60 batches may not be repeated due to accidental errors. Then, we randomly selected 8 samples and all observed a large number of kirigami structures under an Optical Microscope (OM). The large area and regular MoS_2 domains make it possible to calculate the percentage of these kirigami structures fabricated by the space-confined method. Figure S1i shows the average yield of this kirigami structure can reach 50%, even though the nucleation density of each batch is non-uniform, which is difficult to avoid in the growth of

CVD. Therefore, this space-confined method to fabricate the kirigami structure has ideal repeatability, which lays a foundation for the expansion of this technology to other 2D material.

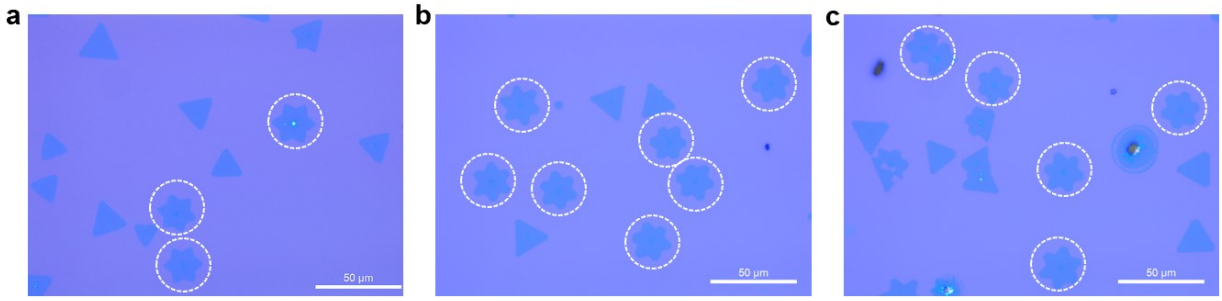

Figure S2. Optical images of the hexagram-shaped first layer formed at the initial growth stage.

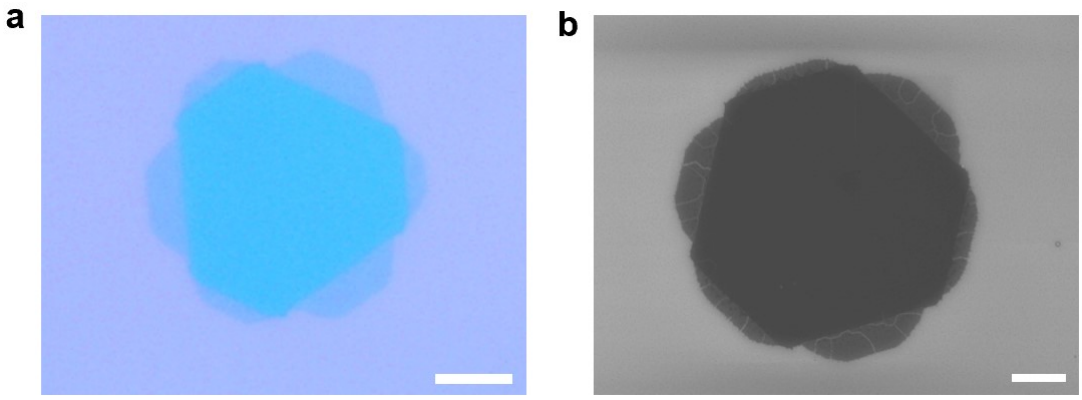

Figure S3. OM and SEM images of MoS_2 kirigami structures at the initial stage of etching. Scale bars are 5 μm.

As shown in Figure S3, the etching behavior of second layer MoS_2 originates from a hexagon structure and subsequently deepens at different precursor ratios. It is worth mentioning that there is a slight distinction in the hexagram-shaped first layer, which may be due to the different rates between the etching and growth. Although the hexagram of the first layer will be slightly different at the apex, but far away from the second layer, which may have its independent etching rules. Furthermore, we found that the bilayer MoS_2 kirigami structures obtained by the two types of etching behaviors both exhibit the same stacking phase (2H phase), and the most important factor affecting the selective etching behaviors is the precursor concentration rather than the morphology of the first layer at the bottom. In this case, we supposed that the first layer has little effect on the second layer etching and follows another etching mechanism.

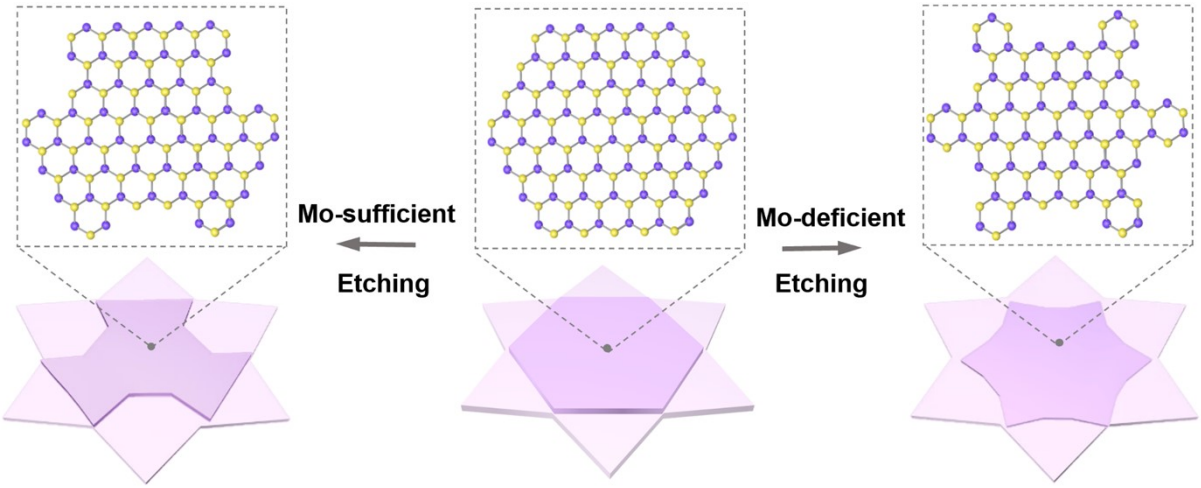

Figure S4. Two types of etching behavior of second layer MoS_2 under different microenvironments.

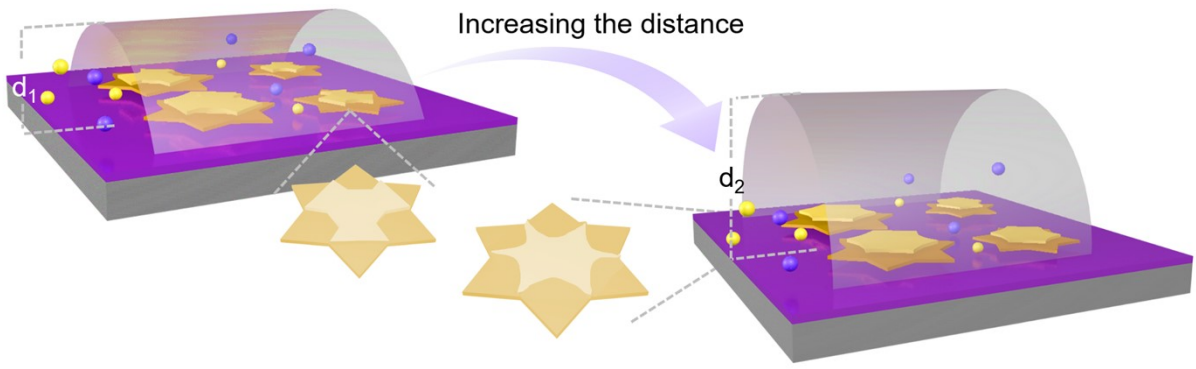

Figure S5. Schematic diagram of the construction confined space by adjusting the distance between Mo foil and substrate.

Figure S5 shows how to construct a confined space by adjusting the distance between Mo foil and substrate. Although, it is challenging to accurately measure the amount of precursors involved in the reaction due to the limitation of high temperature and the instantaneous volatilization of the precursors. Fortunately, the macroscopic crystal morphology during growth allows us to determine the quantitative ratio of atoms involved in the reaction. Specifically, we control the vertical distance from the highest point to the substrate by controlling the length of the Mo foil. Multiple hexagonal crystal structures were observed when the distance was fixed between 3 ~ 5mm (d_1), indicating that the ratio of S and Mo involved in the reaction is 2 according to previous reports. As the reaction progresses, the Mo foil can continuously and stably supply Mo atoms in a confined space, while a large amount of S powder is taken away by the carrier gas Ar, resulting in a Mo-sufficient microenvironment and achieving selective etching of the S-zigzag edges. When the distance was adjusted between 5 mm to 10 mm (d_2), there were different etching behaviors, that is, both Mo-zigzag and S-zigzag edges are etched inward. The carrier gas will take away more Mo atoms, resulting in a decrease in Mo concentration. Thus, we can achieve precursor concentration by adjusting the distance between Mo foil and substrate.

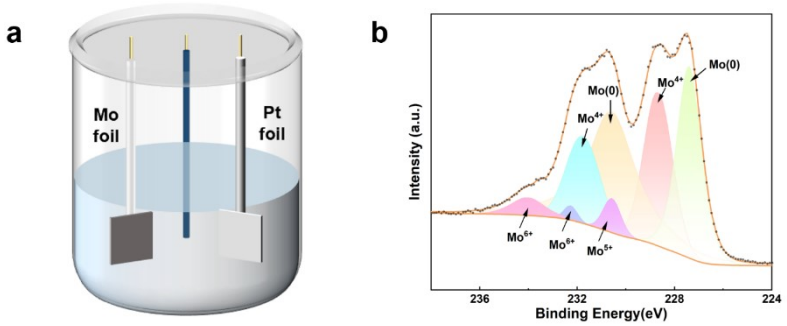

Figure S6. (a) Schematic diagram of electrochemical treatment of Mo foil. (b) XPS results of anodized Mo foil with richer valence states(from IV to VI).

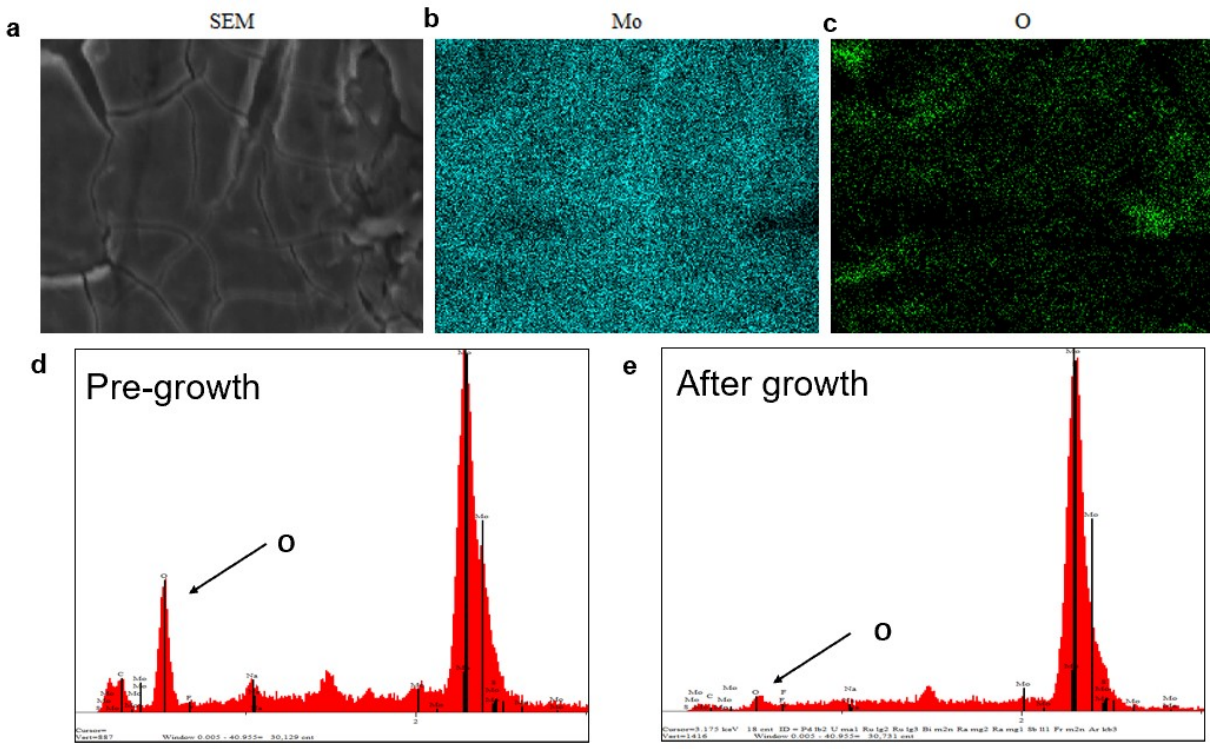

Figure S7. Energy dispersive X-ray spectroscopy (EDX) of pre-growth Mo foil (d) and after-growth Mo foil (e). The disappearance of the O signal indicates that the Mo foil effectively provides Mo atoms.

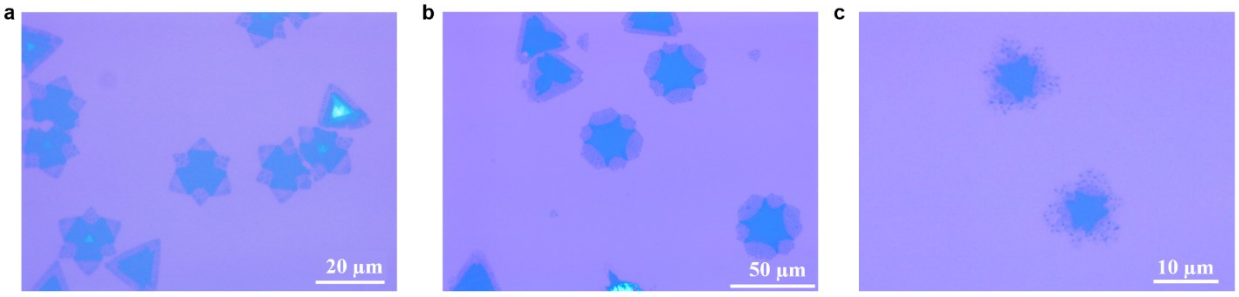

Figure S8. OM images of excessively etched MoS_2 kirigami structure at high temperatures.

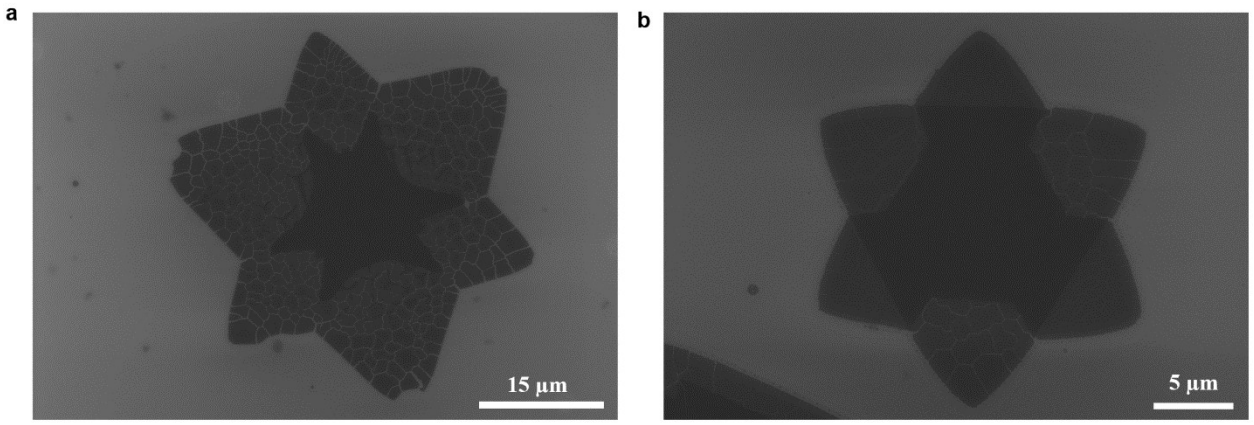

Figure S9. SEM images of excessively etched MoS_2 kirigami structure at high temperatures.

Figures S8 and Figure S9 show the case of excessive etching under high-temperature conditions up to 1100℃, accompanied by cracks in the first layer of MoS_2 and the relative integrity of the second layer. We supposed that this is attributed to the high temperature of the substrate surface making the bottom layer MoS_2 affected more significantly than the second layer.

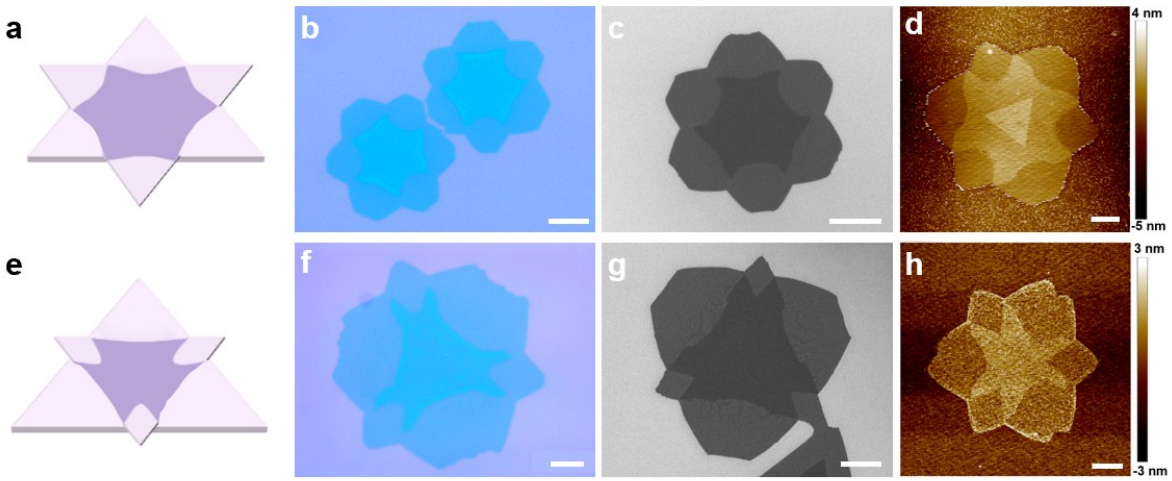

Figure S10. (a-d) Schematic diagram, OM, SEM, and AFM results of symmetrical samples. (e-h) Schematic diagram, OM, SEM, and AFM results of asymmetric samples. Scale bars are 5 μm.

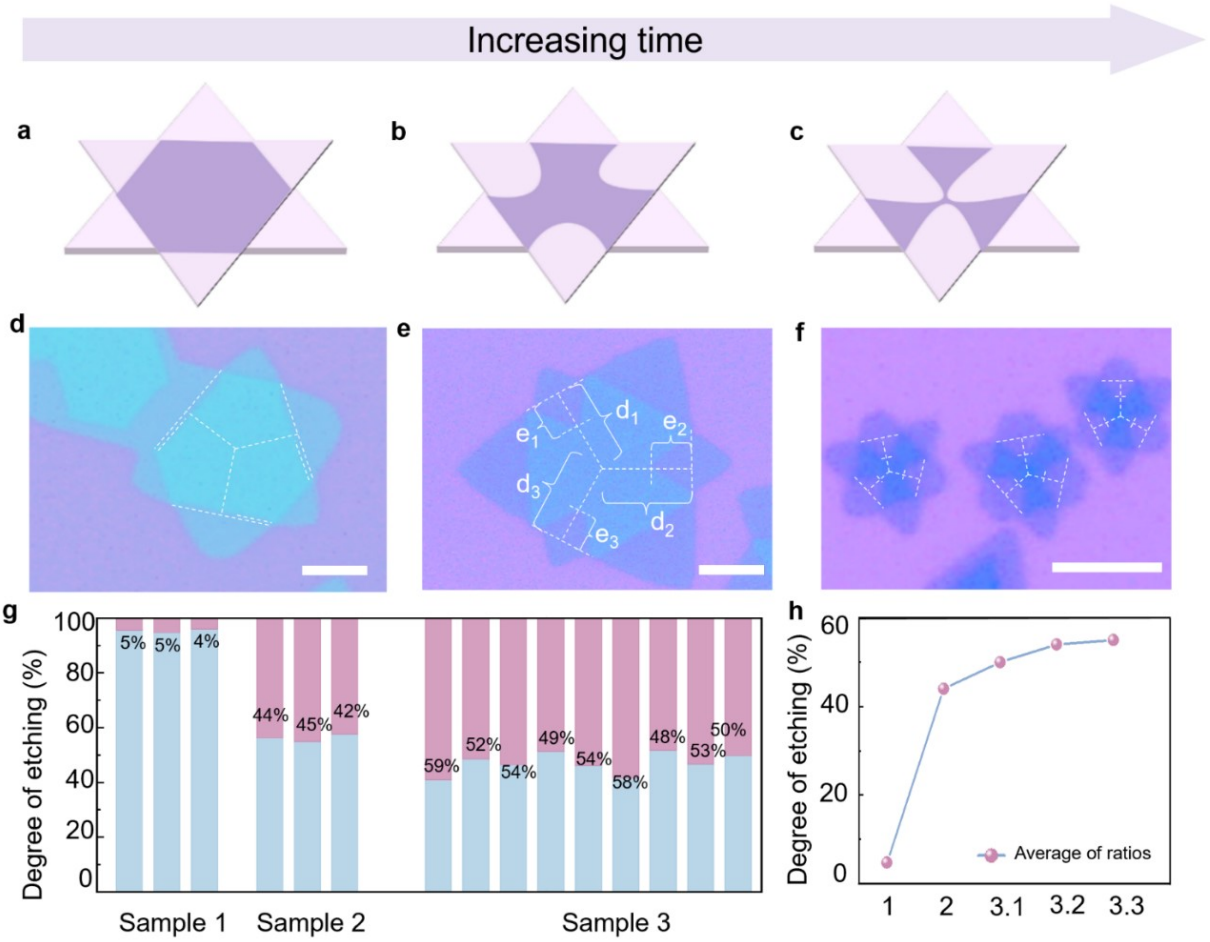

Figure S11. The etching morphology of the second layer of MoS_2 evolves from hexagon to pinwheel with time. (a-c) Schematic diagrams of the degree of etching deepening with time. (d-f) Optical images of kirigami structures at different degrees of etching. The degree of etching is defined as the ratio of the etching depth (e_n) to the intact depth (d_n). (g) Degree of etching of three samples at different stages. Three etched areas of each sample were counted to reduce the errors. (h) The average degree of etching for each sample, showing a deepening trend.

The sharp edges of the kirigami structure enable us to observe the etching boundaries unambiguously. Therefore, we can measure the etching depth under the OM. Firstly, connect

two unetched vertices as shown in Figure S11e. The vertical distance from the line to the kirigami center is defined as d_n, and to the etching boundary is named e_n, (n=1, 2, 3…). We measured the three etching regions of each sample and described the degree of etching by using e_n/d_n, which is positively correlated with the degree of etching. It is worth noting that there are three MoS_2 domains in the optical image of sample 3, and the domain sizes are smaller than sample 1 and sample 2, which may cause errors during measurement. Thus, all three domains are measured, namely Sample 3.1, 3.2, and 3.3. The e_n/d_n average values of the three samples expand sequentially (Sample 1 is 4%, Sample 2 is about 40%, and Sample 3 is about 50%.), as seen in Figures S11g, h, demonstrating a deepening of the degree of etching.

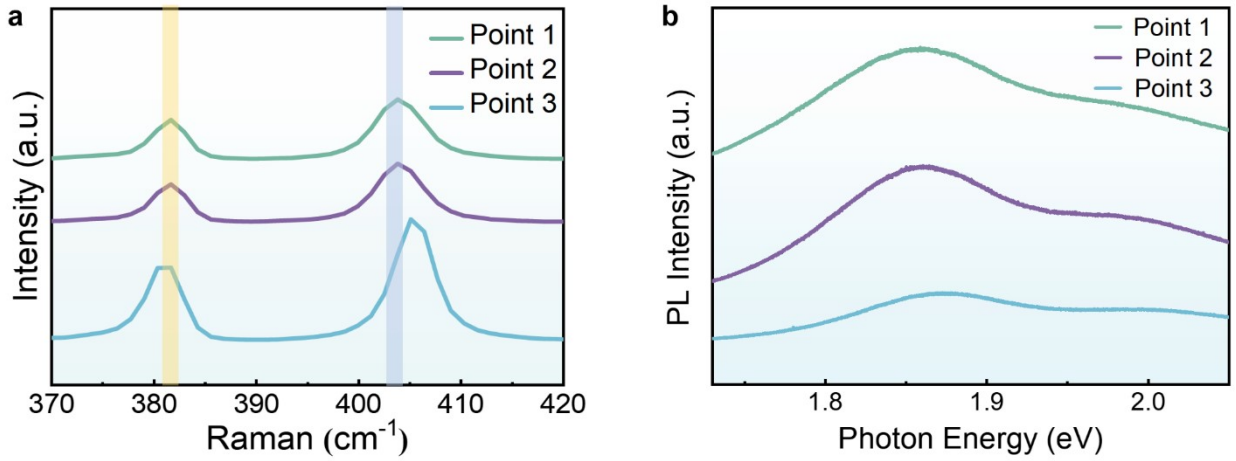

Figure S12. (a) Raman results of Mo/S-zigzag samples from the first layer (point 1), etched area (point 2), and the second layer (point 3). (b) PL results of Mo/S-zigzag samples from the first layer (point 1), etched area (point 2), and the second layer (point 3).

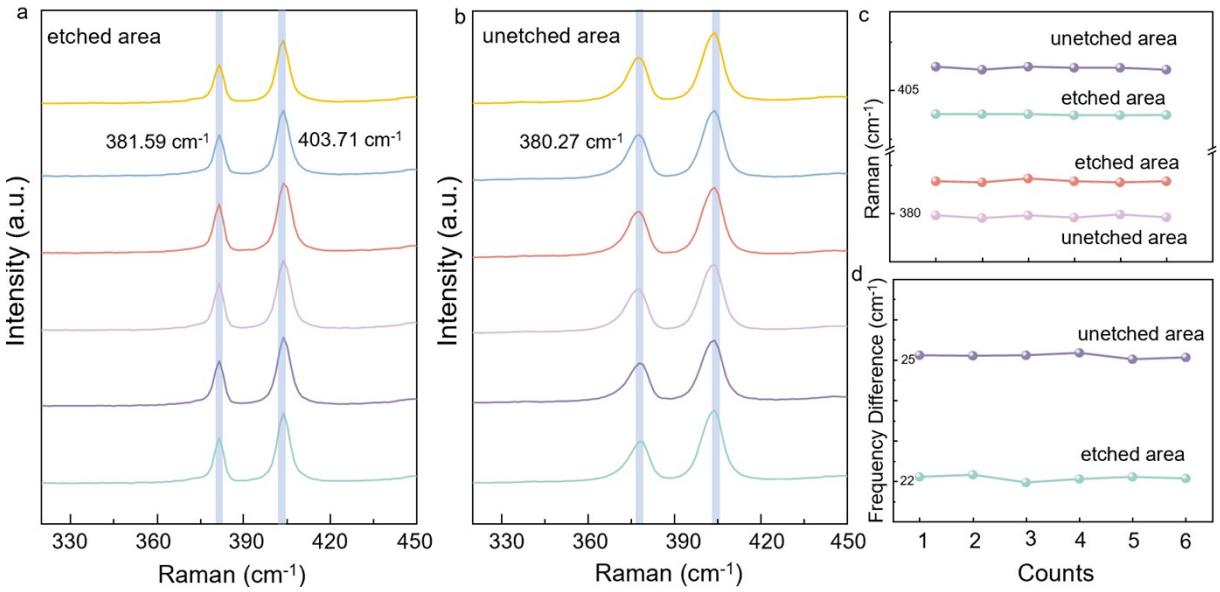

Figure S13. The Raman spectra of the etched and unetched regions across different samples. The etched region exhibits monolayer MoS_2 properties, while the unetched region exhibits bilayer properties.

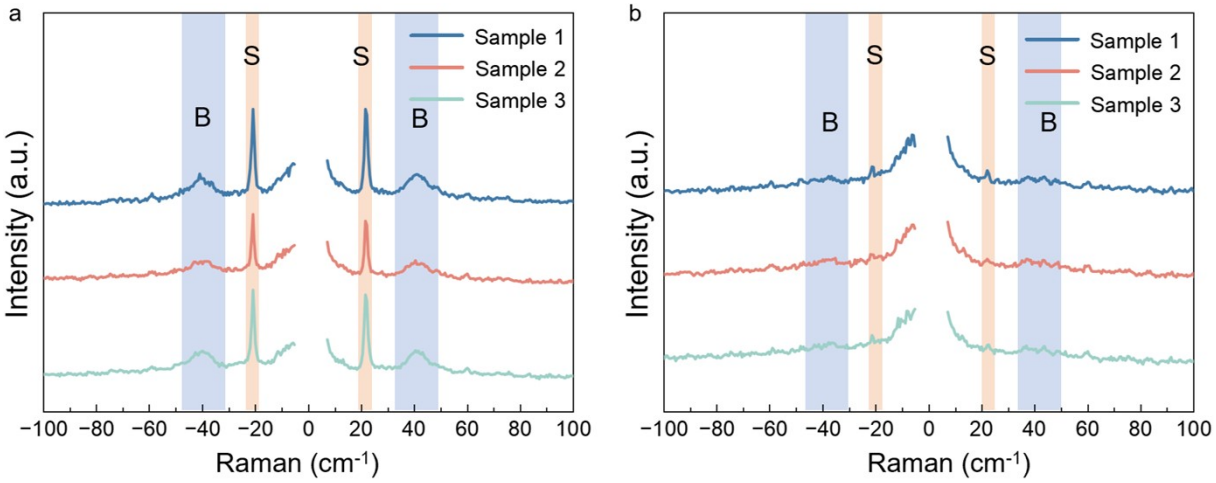

Figure S14. Ultra-low frequency Raman Spectra of MoS_2 kirigami structures from different samples, including interlayer shear (S) and breathing modes (B). (a) The spectra from the unetched region, show the properties of bilayer MoS_2. (b) The spectra from the etched region, show the properties of monolayer MoS_2.

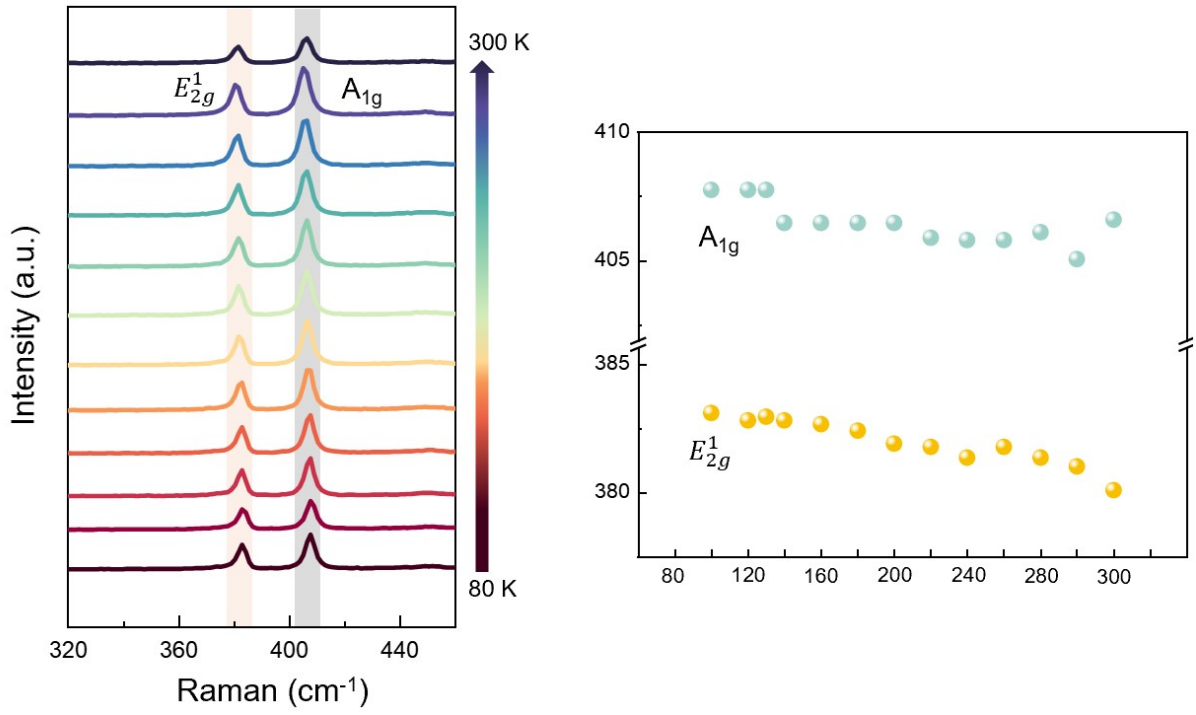

Figure S15. Temperature dependence of peak positions of the E_{2g} and A_{1g} modes for the MoS_2 kirigami structure stored for 12 months, showing a negligible shift.

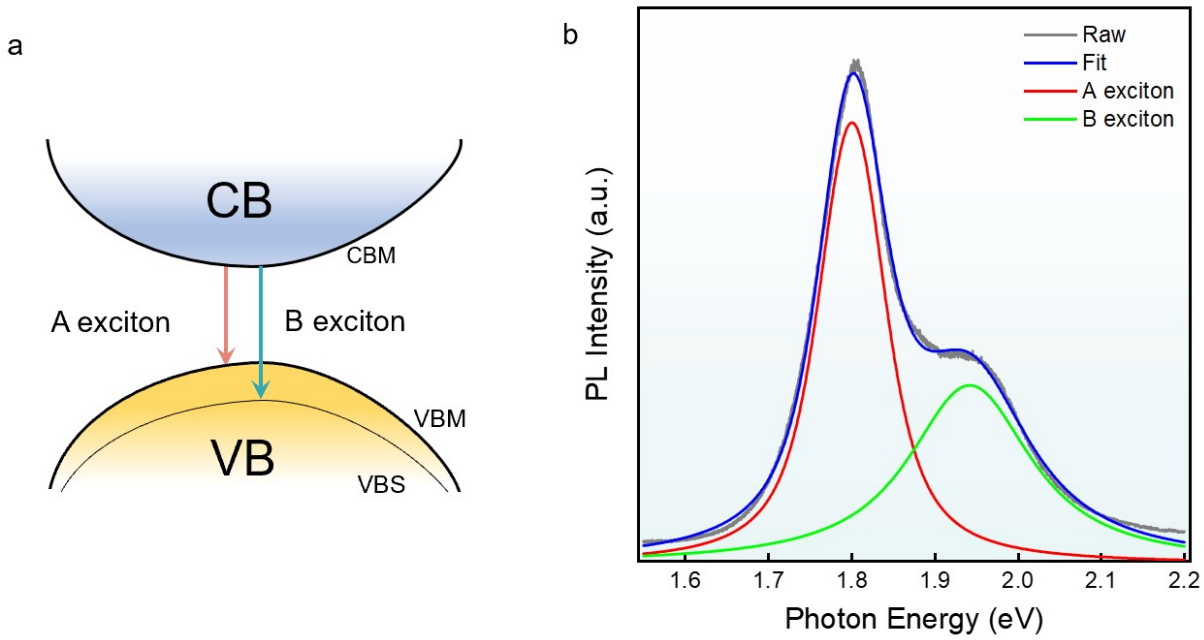

Figure S16. (a) Energy band schematic diagram to show the PL emission process between conduction. (b) PL spectra of MoS_2 kirigami structure stacking region.

As shown in Figure S16, no defect peak was found around 1.7eV. The full width at half maximum (FWHM) of A exciton is about 100 meV and the FWHM of B exciton is about 125 meV, which are influenced by test conditions.

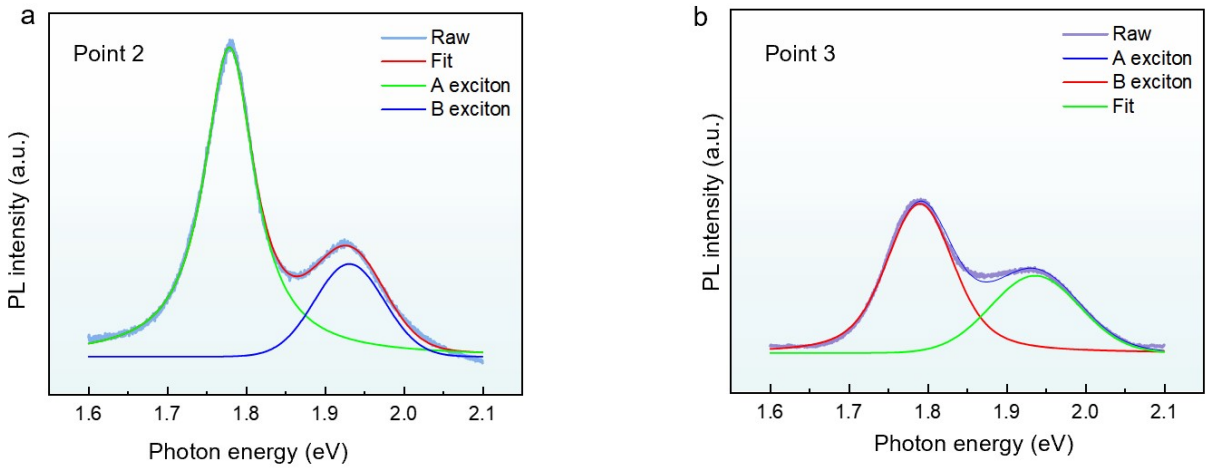

c

	Peak Type	Amplitude (a.u.)	FWHM (meV)	Integral Intensity (a.u.)
Point 2	A exciton	827.245	77	653.997
	B exciton	229.115	104	140.158
Point 3	A exciton	426.420	101	326.856
	B exciton	243.263	133	168.855

Figure S17. (a,b) The PL spectra of point 2 and point 3, were extracted separately to clarify the difference between monolayer and bilayer MoS_2. (c) Integral intensities for A and B excitons in single-layer and bilayer MoS_2 regions. (Integral intensities were calculated by Voigt function deconvolution)

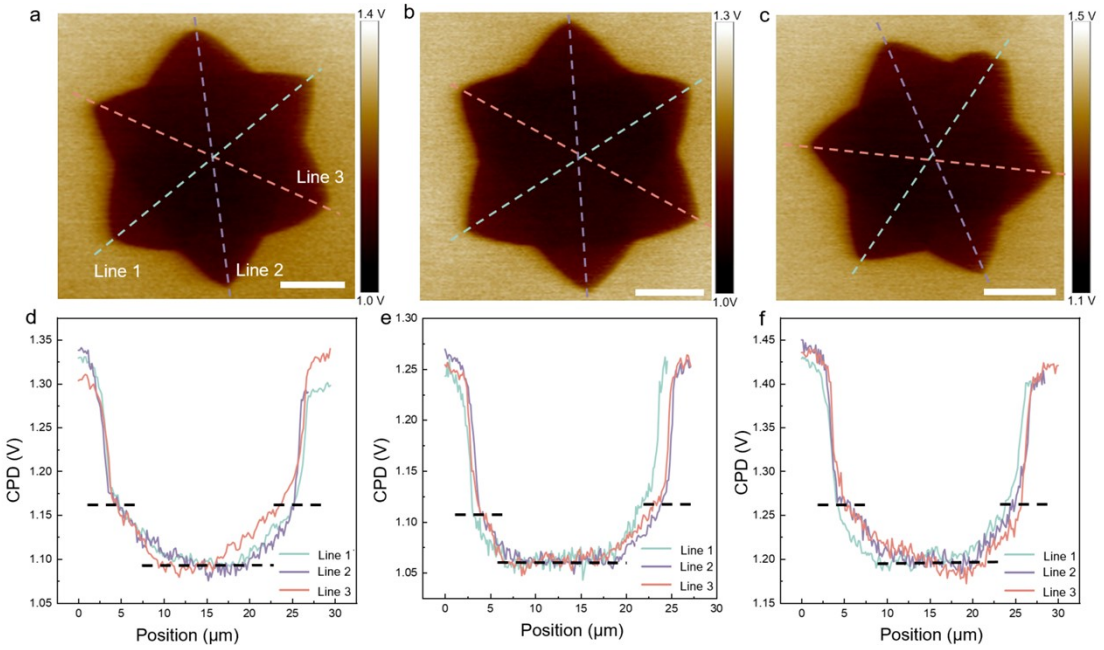

Figure S18. (a-c) KPFM surface potential images of three MoS_2 kirigami structures. (d-f) Surface potential profiles along lines, corresponding to (a-c). Scale bars are 5μm.

Kelvin Probe Force Microscopy (KPFM) is a surface potential measurement technique based on scanning probe microscopy. Capable of operating at the nanoscale, KPFM offers high spatial resolution and provides quantitative measurements of surface potential distributions. This method enables precise characterization of local work function variations and electrostatic properties with nanometer-scale precision. KPFM measures the contact potential difference (CPD) between the sample and the probe using the Kelvin method. By calibrating the probe, the surface potential of the sample can be determined by calculating the difference. In this work, we focus on the variation of the potential over the MoS_2 kirigami structures. Therefore, the measured value is the CPD, which is consistent with the change in the material work function. As shown in Figure S18a-c, the CPD in the central region is significantly reduced, and its general outline is consistent with the kirigami structure observed in the optical microscope. It has been confirmed in the previous results that the central region is bilayer MoS_2, which is an indirect band gap. Compared with monolayer MoS_2, the Fermi level is farther from the top of the valence band, thus showing a lower work function. However, the etched edges are not sharp,

which may be attributed to several factors, including the small potential difference between monolayer and bilayer MoS_2, the limited resolution of the instrument, and the relatively weak influence of the atomic termination boundaries.

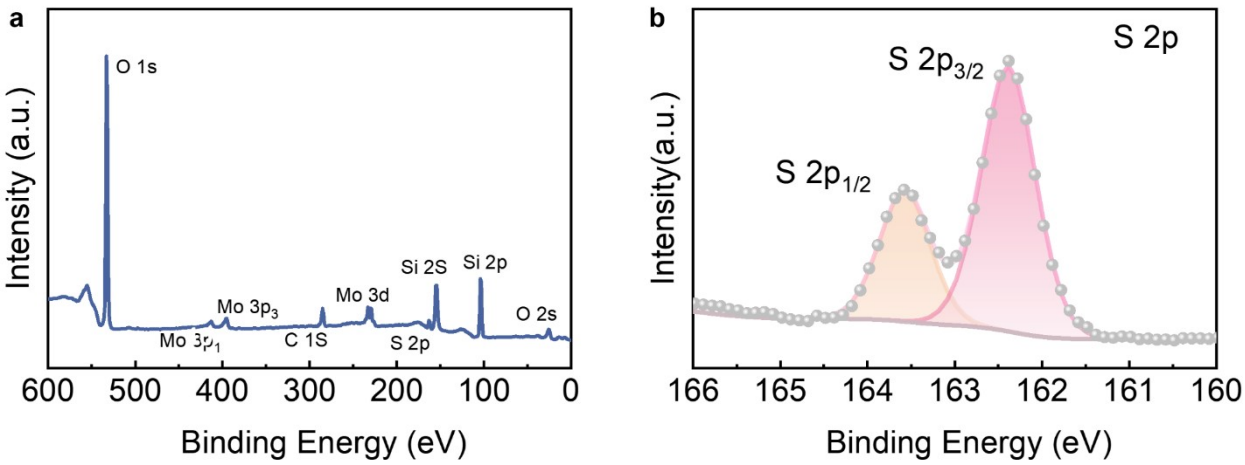

Figure S19. (a) A XPS survey scan of as-etched MoS_2. (b) The XPS core level of S 2p.

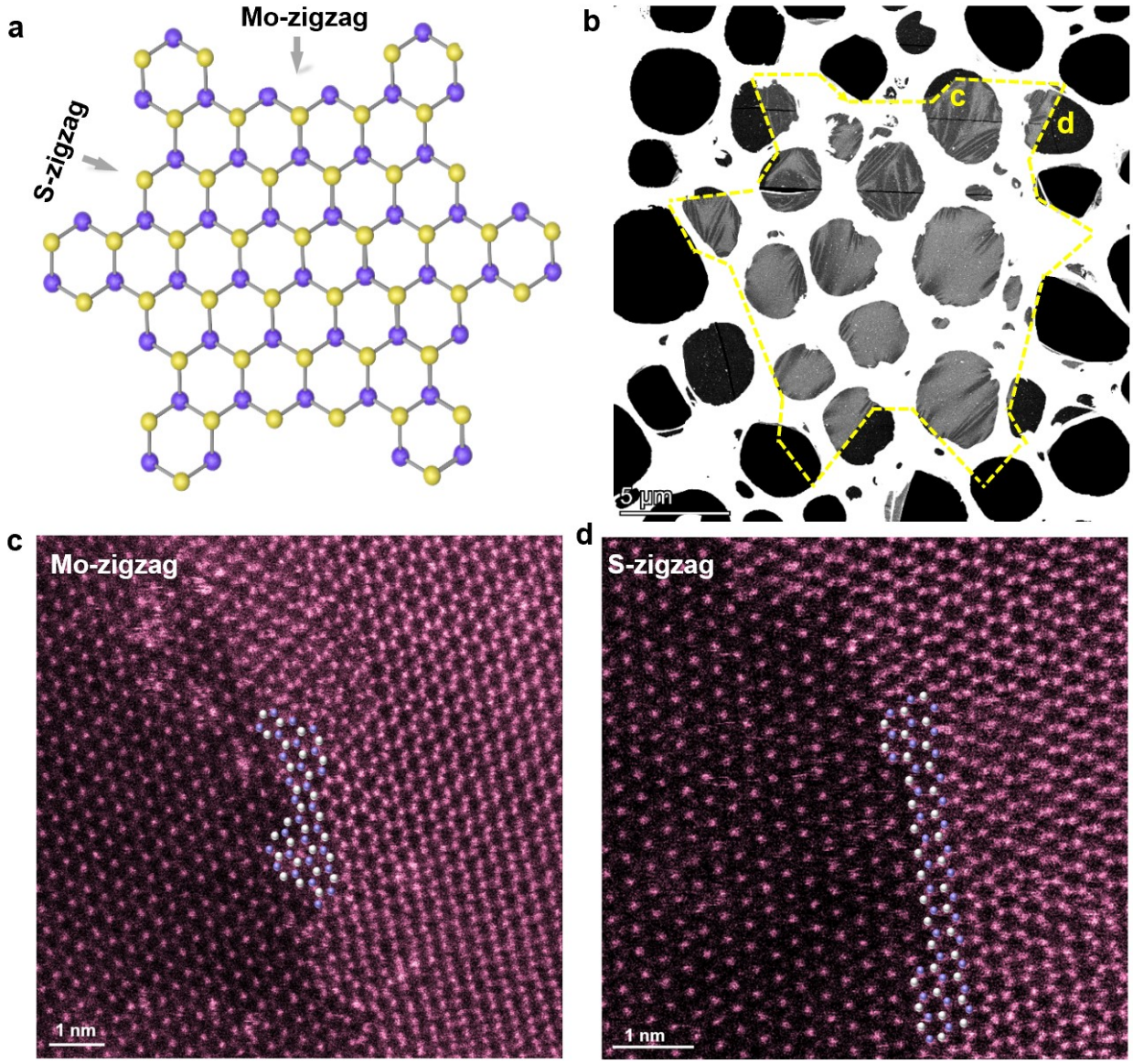

Figure S20. STEM characterization of Mo/S-zigzag etched structure. Both Mo-zigzag and S-zigzag can be observed at etched edges.

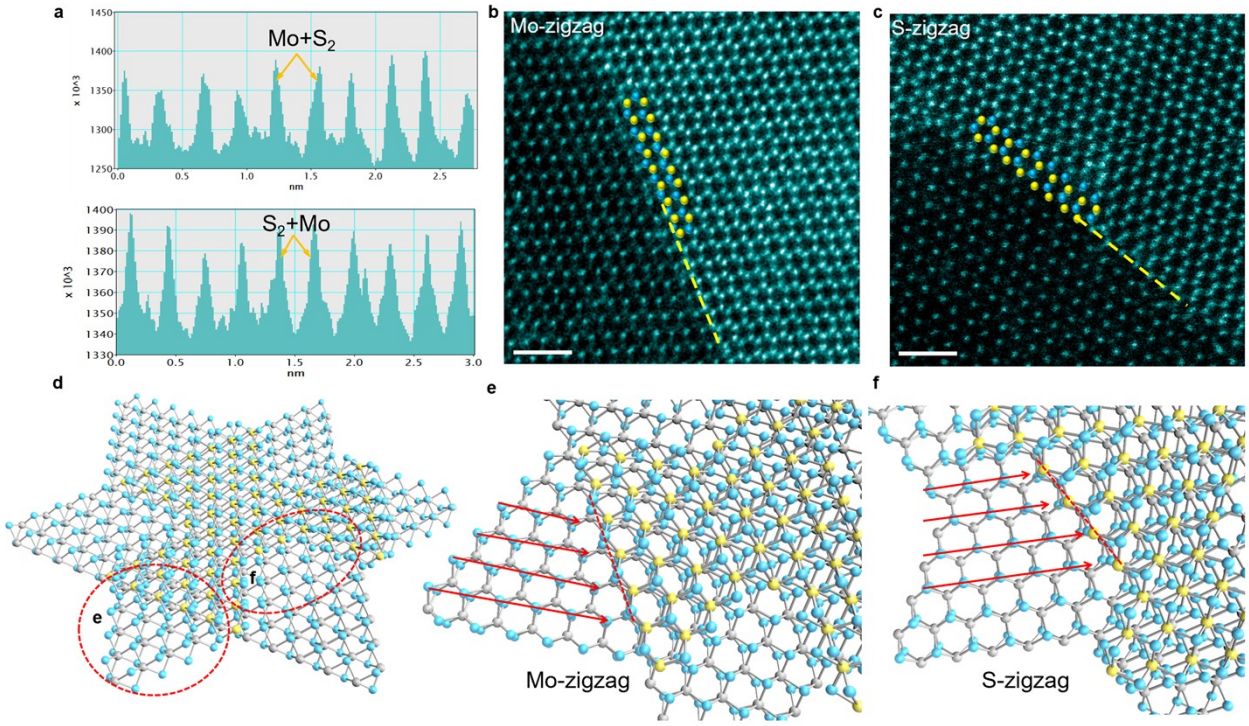

Figure S21. Atomic-resolution HAADF-STEM images of the etched edges of two kirigami structures. (a) The corresponding intensity profile obtained in (b) and (c) along the yellow lines. Scale bars are 1 nm. (d) Schematic illustrations of bilayer MoS_2 kirigami structure and the corresponding unetched boundary (e, Mo-zigzag) and etched boundary (f, S-zigzag)

The corresponding intensity profiles of Mo-zigzag and S-zigzag edges have been provided to clarify the terminal atom in Figure S15a. Nevertheless, each bright spot represents a stacking of two S atoms and one Mo atom ($Mo+S_2$) due to the bilayer MoS_2 kirigami structure being stacked in a 2H phase, which poses a challenge to identifying the types of terminal atoms. Fortunately, on the basis of clear HADDF-STEM images of the monolayer region and sharp etching edges in the second layer, we can derive the atomic arrangement of the boundary along the atomic order of the first layer, as shown in Figure S15d-f. It is obvious in the monolayer MoS_2 region that the bright atom represents Mo atoms, and the dark atoms represent S atoms, exhibiting an ideal honeycomb structure. The S atom in the first layer is represented by gray to make the image clearer in schematic illustrations. The analysis is carried out along the direction

of Mo atoms in the monolayer region. As shown in Figure S15e-f, the Mo atom from the second layer is located at the upper left of the first layer, while the S atom from the second layer is located directly above the first layer of the Mo atom. Therefore, we can distinguish whether the terminal atom is Mo or S.

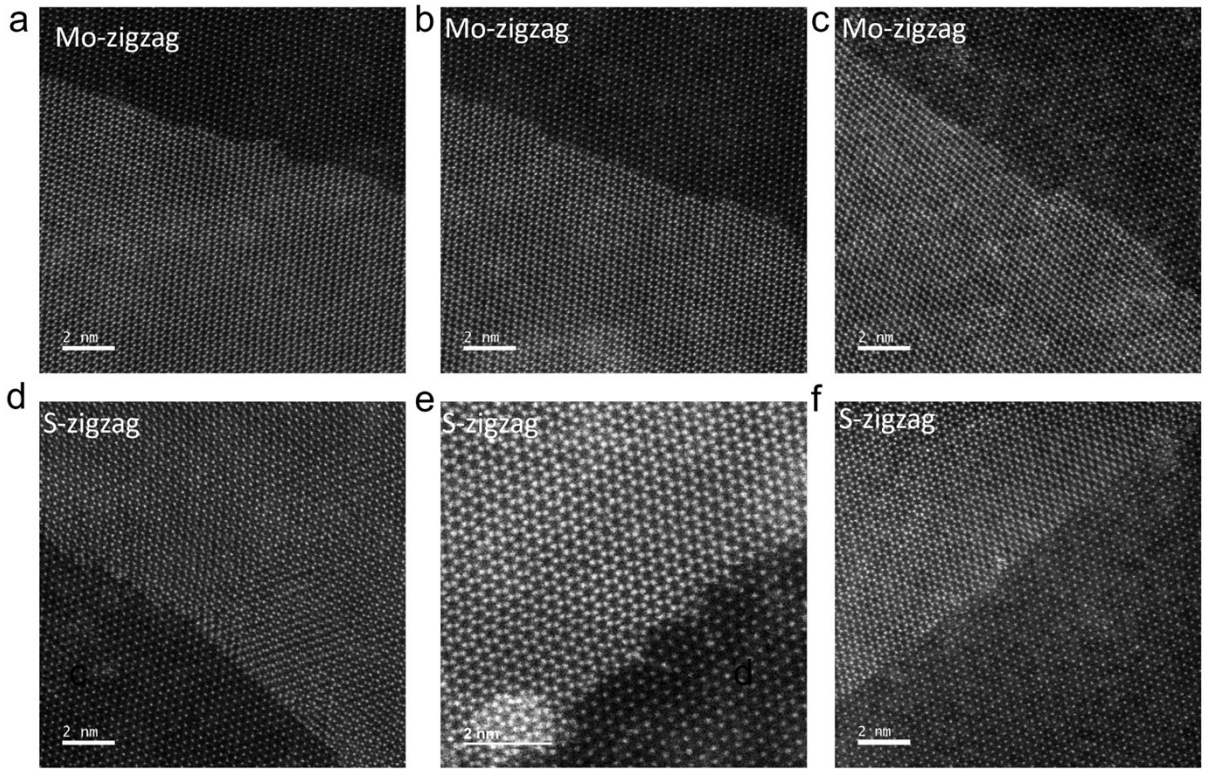

Figure S22. STEM images of Mo-zigzag edges (a-c) and S-zigzag edges (d-f).

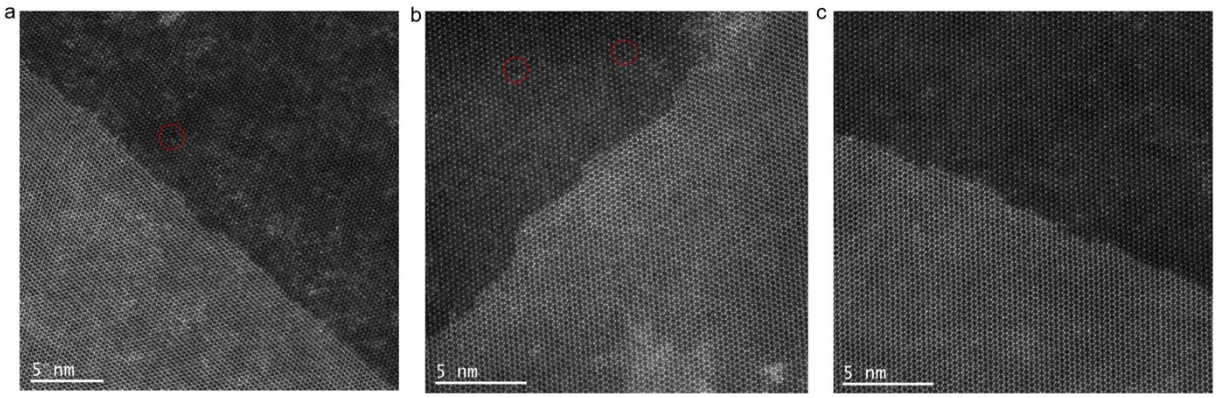

Figure S23. Large-area STEM images of MoS_2 kirigami structures. The structural characterization revealed a highly crystalline material with negligible sulfur vacancy concentration.

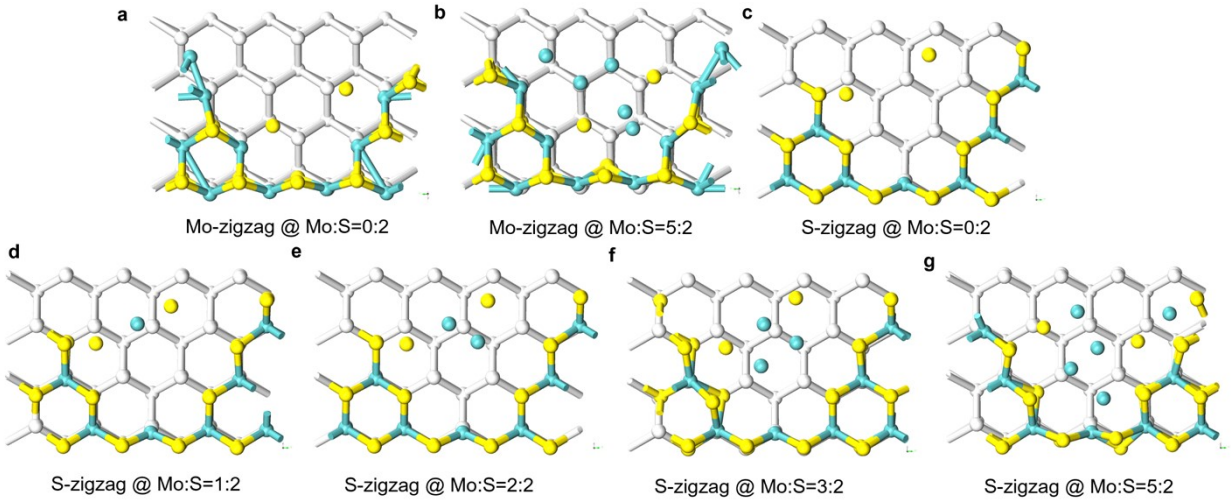

Figure S24. (a-b) Top views of the Mo-zigzag structure at Mo and S concentration ratios of 0:2 and 5:2. (c-g) Top views of the S-zigzag structure at Mo and S concentration ratios of 0:2, 2:2, 3:2 and 5:2.

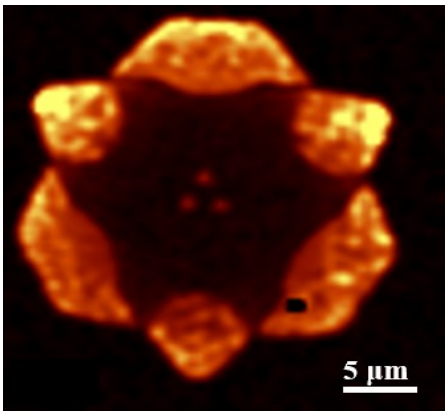

Figure S25. SHG mapping of Mo/S-zigzag etched structure indicating the material is 2H phase.

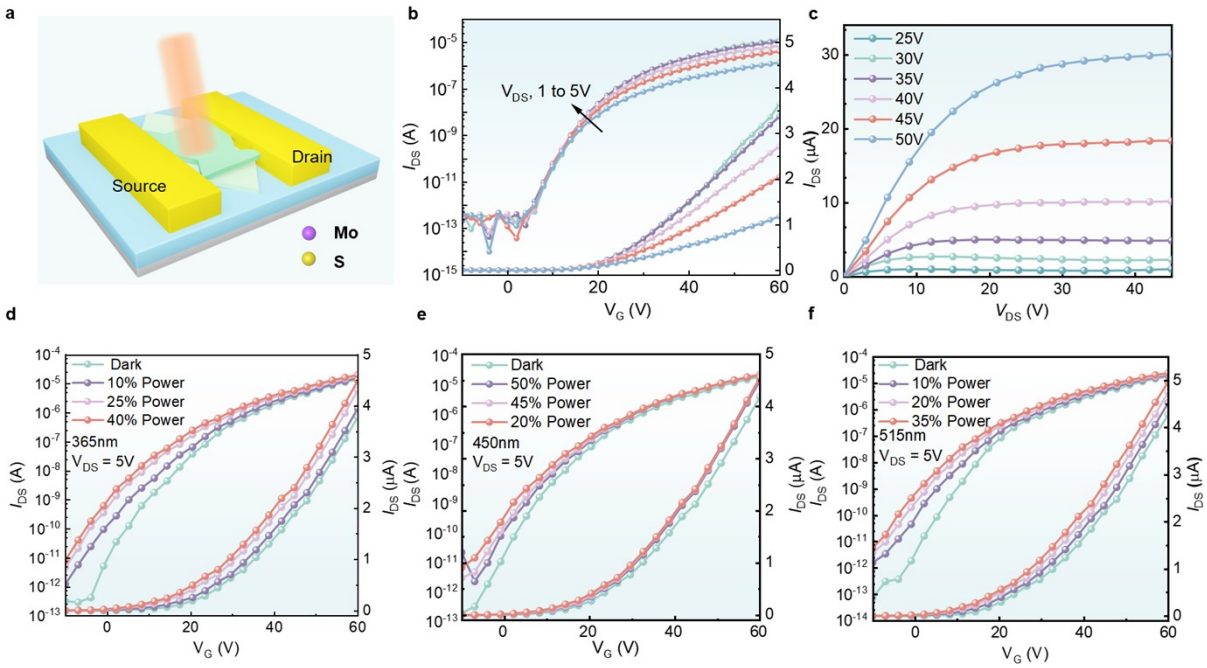

Figure S26. Electrical and optoelectrical properties of the MoS_2 kirigami structure FET devices. (a) Transfer characteristics of the MoS_2 kirigami structure transistors. (b) Output characteristics of the MoS_2 kirigami structure transistors. Transfer characteristics of the MoS_2 kirigami structure transistors under 365 nm (d), 450 nm (e), and 515 nm (f) light illumination.